Anisotropic phonon response of few-layer $PdSe_2$ under uniaxial strain

Weijun Luo[1], Akinola D. Oyedele[2,5], Yiyi Gu[2], Tianshu Li[3], Xingzhi Wang[1], Amanda V. Haglund[5,6], David Mandrus[6,7], Alexander A Puretzky[2], Kai Xiao[2], Liangbo Liang[2], Xi Ling[1,3,4*]*

((Optional Dedication))

Weijun Luo, Dr. Xingzhi Wang, Prof. Xi Ling
Department of Chemistry, Boston University, Boston, MA 02215, United States
E-mail: xiling@bu.edu

Dr. Akinola D. Oyedele, Dr. Yiyi Gu, Dr. Alexander A Puretzky, Dr. Kai Xiao, Dr. Liangbo Liang
Center for Nanophase Materials Sciences, Oak Ridge National Laboratory, Oak Ridge, TN 37831, United States
E-mail: liangl1@ornl.gov

Tianshu Li, Prof. Xi Ling
Division of Materials Science and Engineering, Boston University, Boston, MA 02215, United States

Prof. Xi Ling
The Photonics Center, Boston University, Boston, MA 02215, United States

Dr. Akinola D. Oyedele, Amanda V. Haglund
Bredesen Center for Interdisciplinary Research and Graduate Education, University of Tennessee, Knoxville, TN 37996, United States

Amanda V. Haglund, Prof. David Mandrus
Department of Materials Science and Engineering, University of Tennessee, Knoxville, TN 37996, United States

Prof. David Mandrus
Materials Science and Technology Division, Oak Ridge National Laboratory, Oak Ridge, TN 37830, United States

Keywords: ((transition metal dichalcogenides, $PdSe_2$, strain engineering, Raman spectroscopy, stretchable))

Abstract

$PdSe_2$, an emerging two-dimensional (2D) material with a novel anisotropic puckered pentagonal structure, has attracted growing interest due to its layer-dependent electronic bandgap, high carrier mobility, and good air stability. Herein, a detailed Raman spectroscopic study of few-layer $PdSe_2$ (two to five layers) under the in-plane uniaxial tensile strain up to 3.33% is performed. Two of the prominent $PdSe_2$ Raman peaks are influenced differently depending on the direction of strain application. The A_g^1 mode redshifts more than the A_g^3 mode when the strain is applied along the *a*-axis of the crystal, while the A_g^3 mode redshifts more than the A_g^1 mode when the strain is applied along the *b*-axis. Such an anisotropic phonon response to strain indicates directionally-dependent mechanical and thermal properties of $PdSe_2$, and also allows the identification of the crystal axes. The results are further supported by first-principles density functional theory (DFT). Interestingly, the near-zero Poisson's ratios for few-layer $PdSe_2$ are found, suggesting that the uniaxial tensile strain can be easily applied to few-layer $PdSe_2$ without significantly altering their dimensions at the perpendicular directions, which is a major contributing factor to the observed distinct phonon behavior. The findings pave the way for further development of 2D $PdSe_2$-based flexible electronics.

Introduction

Anisotropic two-dimensional (2D) layered materials such as black phosphorus,[1,2] ReS_2 [3,4], and many other candidates [5–11] show directionally-dependent physical properties such as mechanical flexibility,[13] thermal conductivity [14–17] and optical responsivity.[18–20] Pentagonal $PdSe_2$, a transition metal dichalcogenide (TMDC), has recently joined this 2D family.[21,22] Compared to black phosphorus, $PdSe_2$ shows a similar layer-dependent electronic bandgap, with enhanced stability in air, which is advantageous for future device fabrication. Compared to many other members in this family, $PdSe_2$ features higher carrier mobilities and current on/off ratios.[21,22] In addition, by introducing defects into $PdSe_2$ under plasma irradiation, a structural phase transformation occurs from semiconducting $PdSe_2$ to metallic $Pd_{17}Se_{15}$ that could increase the carrier mobility in $PdSe_2$ transistors by nearly 20 times compared to the transistors using Ti/Au electrodes.[23] Growing research interests have been focused on its broad potentials for application in electronics,[21] photovoltaics,[24,25], and thermoelectrics.[26] However, the effect of strain in $PdSe_2$ has been relatively underexplored. Understanding the anisotropic physical properties of $PdSe_2$ can provide the key foundation for the future design of flexible $PdSe_2$-based devices.

Raman spectroscopy is a powerful characterization tool for studying the physical properties of anisotropic 2D materials. It has been widely used to determine the crystallographic orientations,[2,5,27–29] layer numbers,[30–39], and strains of various 2D materials.[40–48] In particular, the phonon response under strain was found to be anisotropic in several anisotropic 2D materials such as black phosphorus and $ReSe_2$.[45,49,50] Recently, Akinola et al. reported the Raman spectra of layered $PdSe_2$ [21], and the observed phonon modes were used to identify the numbers of layers.[51] Nevertheless, the experimental investigations on the phonon response of strained $PdSe_2$ are still lacking, which, however, is crucial for the integration of few-layer $PdSe_2$ into flexible electronic devices.

In this work, we experimentally studied the phonon response of 2 – 5 layers (L) $PdSe_2$ under uniaxial tensile strain loading up to 3.33% by using the angle-resolved polarized Raman spectroscopy. Focusing on the two characteristic Raman modes A_g^1 and A_g^3, the phonon frequency of A_g^1 mode decreases more than that of the A_g^3 mode under strain applied along the *a*-axis of $PdSe_2$, while the A_g^3 mode redshifts more than the A_g^1 mode under strain applied along the *b*-axis of $PdSe_2$. Our results show that $PdSe_2$ exhibits an anisotropic phonon response to strain, like other anisotropic 2D materials (such as black phosphorus and $ReSe_2$). The anisotropic phonon-strain relation helps to understand the directionally-dependent mechanical and thermal properties. It also allows the determination of the crystal axes, a necessary step for many practical applications of anisotropic 2D materials. We further performed first-principles density functional theory (DFT) simulations of strained 1 – 3L $PdSe_2$ to understand the microscopic origin of this distinct phonon behavior. We found near-zero Poisson's ratios under the uniaxial tensile strain, suggesting that the tensile strain applied in $PdSe_2$ is effectively uniaxial. In contrast, for many other anisotropic 2D materials such as black phosphorus, the Poisson's ratios are notably larger,[45] and hence a compressive strain is automatically induced perpendicular to the applied tensile strain direction, leading to an effective biaxial strain in the system. The near-zero Poisson's ratio in few-layer $PdSe_2$ is a major factor contributing to the observed anisotropic phonon response. The advantage of a near-zero Poisson's ratio is that the strain in $PdSe_2$ can be easily controlled to focus on a particular direction, which would allow the strain application for $PdSe_2$ flexible electronics to be more controllable compared to 2D materials with large Poisson's ratios. Our experimental and theoretical findings are expected to facilitate further understanding of the mechanical, thermal, optical and electronic properties of $PdSe_2$ for future flexible electronics.

Results and Discussions

Figure 1 (A) shows the crystal structure of $PdSe_2$, where the unique pentagonal structure is clearly seen. A single layer of $PdSe_2$ has a periodic corrugated structure where each Pd atom is connected with four Se atoms, and each Se atom is bonded with two Pd atoms and another Se atom. The two major crystal axes ([100] and [010]) of $PdSe_2$ are along the *a* and *b* directions in the 2D plane, respectively. The bulk $PdSe_2$ crystals exhibit Pbca (#61) space group symmetry and D_{2h} point group symmetry. Due to the symmetry reduction from bulk to few-layer $PdSe_2$, the odd *n*L $PdSe_2$ belongs to space group $P2_1/c$ (#14) and point group C_{2h} (2/m); the even *n*L $PdSe_2$ belongs to space group $Pca2_1$(#29) and point group C_{2v} (mm2), where *n* is the number of layers.[51]

$PdSe_2$ flakes were prepared using mechanical exfoliation from single-crystalline bulk $PdSe_2$. **Figure 1** (B) shows the transmission electron microscopy (TEM) image of a relatively thick (> 20 L) $PdSe_2$ flake where the long and short edges of the near rectangular shape flake were clearly seen. From the HRTEM (high-resolution TEM) images in **Figure 1** (C), we determined the crystallographic orientations of the $PdSe_2$ flake, where the long and short edges of the $PdSe_2$ flake pointed to the *a* ([100] direction) and *b* axes ([010] direction), respectively. The lattice plane spacing of 0.286 nm corresponds to the $PdSe_2$ (200) lattice planes.[52] The inset fast Fourier transformation (FFT) pattern shows the (200) and (020) lattice planes.

The angle-dependent Raman responses of this flake were investigated under a parallel configuration ($P_i//P_s$, P_i, and P_s are the polarization of the incident and scattered light), where the sample was rotated to change the angle (θ) between the crystallographic orientation and the polarization of the incident light. As shown in **Figure 1** (D), under 532 nm laser excitation, the typical Raman spectra collected at θ = 0° (incident polarization parallel to the *a*-axis) and θ = 90° (incident polarization parallel to the *b*-axis) showed the A_g^1, A_g^2 and A_g^3 modes at 143, 205, and 256 cm^{-1}, respectively, where the mode assignments were given in the literature.[21,51]

Figure 1 (E) shows the contour color map of the Raman intensity changes with respect to θ, where we found the maximum (minimum) A_g^1 intensity appeared when the incident polarization was parallel to the *a*-axis (*b*-axis). The polar plots of the Raman intensity as a function of θ and detailed Raman tensor analysis were shown in **Section** S1. Moreover, the TEM and angle-resolved Raman spectra of five more thick $PdSe_2$ flakes with different thicknesses were shown in **Figure** S3 – S7 in the SI, whose A_g^1 modes showed the same behavior that the maximum (minimum) intensity appeared when the incident polarization was parallel to the *a*-axis (*b*-axis) axis. In other words, under 532 nm excitation, the direction of the maximum A_g^1 Raman intensity is thickness-independent. Thus, we can use the anisotropic Raman scattering of the A_g^1 mode to identify the crystallographic orientation for the strain study in this work.

Figure 2 (A) shows an exfoliated $PdSe_2$ sample on a 300 nm SiO_2/Si substrate. Note that different numbers of layers of $PdSe_2$ exist in one flake, indicating that their crystallographic orientations are the same. Their thicknesses were determined using the low frequency (LF) Raman spectra of interlayer vibration modes (**Figure S8** (C) and S8 (D) in the SI), which has been proved to be an accurate and effective method for fast and unambiguous identification of the number of layers of $PdSe_2$ and many other 2D materials.[39,51] The angle-resolved Raman spectra under 532 nm laser excitation further confirmed the crystallographic orientation of the thick region of flake (**Figure** S8 (A)): the A_g^1 mode maximum intensities all appeared at 0°, corresponding to the *a*-axis of the $PdSe_2$ crystal, and the *b*-axis was identified to be along 90°. The $PdSe_2$ flake was then transferred from the SiO_2/Si substrate to a cross–shape flexible polyimide substrate for strain-related studies. **Figure 2** (B) illustrates the alignment of the $PdSe_2$ sample and the straining process. The *a* and *b* axes of the $PdSe_2$ flake were aligned with the two intersecting directions of the flexible substrate, allowing the uniaxial tensile strain to be loaded. The strain was applied to the *a* and *b* axes by stretching the two intersecting directions of the polyimide substrate. The efficiency of the strain applied to the sample was tested and estimated

to be ~ 90 % (See more details in **Section** S10 of SI). Due to the atomically thin nature of the few-layer crystal, the out-of-plane deformation (shear strain) could be regarded as negligible.[45] We measured the Raman spectra of few-layer (2 – 5 L) $PdSe_2$ with the uniaxial tensile strain loading up to 3.33% with an increment of 0.83% along both the *a* and *b* axes of $PdSe_2$. The incident polarization was kept parallel to the strain direction, and the analyzer was taken out to observe the frequency changes of Raman modes with both A_g and B_g symmetries. Note that the Raman signals of the few-layer $PdSe_2$ on the flexible substrate were generally weaker than those on the SiO_2/Si substrate due to the weaker reflection of the Polyimide substrate. For instance, the Raman signals vanished for monolayer $PdSe_2$; for 2L $PdSe_2$, the A_g^1 mode vanished when the incident polarization was parallel to the $PdSe_2$ *b*-axis. In **Figure** 2 (D), the Raman spectra of a 3L $PdSe_2$ under the uniaxial tensile strain along *a*-axis shows the low frequency "B1" mode, two A_g, A_g^1-B_{1g}^1, and A_g^3-B_{1g}^3 modes at 29, 121, 130, 148 and 262 cm^{-1}, respectively, which matched with the previous reports.[21,51]. The A_g^1 mode is very close to B_{1g}^1 mode (a frequency difference of less than 2 cm^{-1}), and they often appear as a single asymmatric peak, denoted as A_g^1-B_{1g}^1.[21] Similarly, B_{1g}^3 mode also shows as a right shoulder peak next to A_g^3 mode.[21] Voigt fitting was thus carried out to differentiate A_g^1 and B_{1g}^1 modes, as well as A_g^3 and B_{1g}^3 modes (see more details in **Figure** S9). In the main text, the frequency shifts were observed for the two most prominent Raman peaks, A_g^1 and A_g^3 modes, which originate from the out-of-plane vibrations of the Se atoms (**Figure 2** (C)). With respect to the uniaxial tensile strain along *a*-axis, the frequencies of both A_g^1 and A_g^3 modes of 3L $PdSe_2$ decreased with the change rates ($\frac{\partial\omega}{\partial\varepsilon}$) of -0.97 cm^{-1}/% and -0.38 cm^{-1}/%, respectively (see **Table** 1). However, when the uniaxial tensile strain was applied along the *b*-axis (**Figure 2** (E)), the A_g^3 mode red-shifted with an increased $\frac{\partial\omega}{\partial\varepsilon}$ of -0.74 cm^{-1}/%, while that of the A_g^1 mode was reduced to -0.25 cm^{-1}/%. Similar directionally-dependent trends of frequency

change were observed for all the other thicknesses studied. **Figure 3** (A) and 3 (B) plot the frequencies of A_g^1 and A_g^3 modes of the 2 – 5 L $PdSe_2$ under the uniaxial strain applied along the $PdSe_2$ *a*-axis. Both modes red-shifted and the A_g^1 mode has relatively larger change rates $\left|\frac{\partial\omega}{\partial\varepsilon}\right|$. However, as shown in **Figure** 3 (C) and 3 (D), when the uniaxial strain was applied along the *b*-axis of $PdSe_2$, the A_g^3 mode red-shifted with much larger change rates $\left|\frac{\partial\omega}{\partial\varepsilon}\right|$ than those of the A_g^1 mode. The frequency change rates ($\frac{\partial\omega}{\partial\varepsilon}$) of A_g^1 and A_g^3 modes of 2 – 5 L $PdSe_2$ were also summarized in **Table** 1, where we observed thickness-dependent frequency change rates for both phonon modes. This will be further discussed in the DFT calculations below. The experimental results clearly suggest anisotropic phonon behaviors under the uniaxial tensile strain along different directions, which can also be used to identify the crystalline orientations of $PdSe_2$, complementary to the angle-dependent Raman intensities of the A_g^1 mode discussed above.

It is interesting to note that with increasing uniaxial tensile strain, the A_g^1 and A_g^3 peaks become broader, as shown in **Figure 2** (D) and (E). We also recorded that the intensities of both A_g^1 and A_g^3 peaks generally decrease with respect to increasing strain (see Figure S12 in the SI). The broadening of linewidth and decreasing of the intensity of $PdSe_2$ A_g^1 and A_g^3 peaks under uniaxial tensile strain were similar to those of the WSe_2 A' and 2LA modes,[48] which could be explained by the change of the polarizability as well as the details of the electronic structure and electron-phonon coupling under strain. We also discussed the influence of the layer number and strain on the electronic band structure (See more details in Section S4 in the SI). Note that the excitation wavelength of 532 nm (2.33 eV) is above the bandgap values of all $PdSe_2$ layers and probably satisfies the condition of resonant Raman scattering in this work. Moreover, it was found that A_g^1 (see **Table** 1) and B_{1g}^1 modes (summarized in **Table** S4 in the SI) exhibit different frequency change rates with strain, which contributes to the linewidth change of the

A_g^1-B_{1g}^1 mixed peak with strain. Similar results were found for A_g^3 and B_{1g}^3 modes (more details in **Table** 1 and **Table** S4). Moreover, the different frequency change rates with strain were caused by the different anharmonicity of the two vibrational modes, where their phonon Grüneisen parameters were analyzed and summarized in **Table S7** of SI.

To understand the different trends of the $\frac{\partial\omega}{\partial\varepsilon}$ along the two axes, DFT calculations were carried out to simulate the $\frac{\partial\omega}{\partial\varepsilon}$ of strained 1 – 3L $PdSe_2$. We first calculated the Poisson's ratio as a function of the uniaxial tensile strain for 1 - 3 L $PdSe_2$ (**Figure S15** in the SI), where Poisson's ratio is defined as $\nu = -\frac{\varepsilon_2}{\varepsilon_1}$, where ε_1 is the tensile strain applied along one direction and ε_2 is the compressive strain induced in the perpendicular direction. Poisson's ratio governs the structural change during the strain and then contributes to the complex frequency changes in anisotropic 2D materials.[45,53] The calculated Poisson's ratios of 1 – 3 L $PdSe_2$ were generally less than 0.08 regardless of the applied strain direction, where the data for 1L $PdSe_2$ was in agreement with recent theoretical work.[54] Note that the Poisson's ratios of black phosphorus are significantly larger (0.85 and 0.19 for $\varepsilon \parallel$ zigzag and $\varepsilon \parallel$ armchair, respectively[45]), and thus the compressive strain is often automatically induced in the perpendicular direction to the applied tensile strain, leading to a biaxial strain in the system, which complicates the phonon response of black phosphorus to the external uniaxial tensile strain due to the involvement of the unintended compressive strain.[45] However, the near-zero Poisson's ratios in $PdSe_2$ suggest that the unintended compressive strain is negligible, and it ensures that the uniaxial tensile strain is applied to the system. Therefore, $PdSe_2$ offers a great platform for the study of the uniaxial strain effect on the Raman scattering.

We then calculated the phonon frequencies of 1 – 3 L $PdSe_2$ under strain. As shown in **Figure 4** (A), 4 (B) and **Table** 2, when the uniaxial tensile strain was applied along the $PdSe_2$ *a*-axis, the A_g^1 and A_g^3 modes both shifted to the lower frequency, where the A_g^1 mode has a

larger $\left|\frac{\partial\omega}{\partial\varepsilon}\right|$ than the A_g^3 mode. **Figure 4** (C) and 4 (D) show when the uniaxial tensile strain was applied along the $PdSe_2$ *b*-axis, though the A_g^1 and A_g^3 modes still both shifted to the lower frequency, the A_g^3 mode has a larger $\left|\frac{\partial\omega}{\partial\varepsilon}\right|$than the A_g^1 mode. Moreover, as shown in **Table 2**, under the presence of strain, the $\left|\frac{\partial\omega}{\partial\varepsilon}\right|$ for both A_g^1 and A_g^3 modes increase with the layer number, suggesting the thickness-dependent strain response, which is in agreement with the experimental results in **Table 1**. The relationship between the $\left|\frac{\partial\omega}{\partial\varepsilon}\right|$ for the A_g^1 and A_g^3 modes along the two axes obtained from our simulations are in qualitative agreement with that observed experimentally (see **Figure 3** and **Table 1**). Nonetheless, the calculated values of $\left|\frac{\partial\omega}{\partial\varepsilon}\right|$ were generally larger than those obtained from experiments. Especially when under the uniaxial tensile strain along the $PdSe_2$ *b*-axis, the experimental $\frac{\partial\omega}{\partial\varepsilon}$ of the A_g^1 and A_g^3 modes were about -0.25 $cm^{-1}/\%$ and -0.74 $cm^{-1}/\%$, respectively for 3L $PdSe_2$, where the $\left|\frac{\partial\omega}{\partial\varepsilon}\right|$ were much smaller than the calculated values. Note that the calculated values of $\left|\frac{\partial\omega}{\partial\varepsilon}\right|$in black phosphorus are also generally larger than the experimental values.[45] Such numerical mismatch is partially contributed to certain approximations embedded in the DFT methodology. Additionally, the experimental conditions (e.g., the effective local temperature discussed in **Section 10** of SI, substrate effect[55] and loading efficiencies [56,57]) are not considered in DFT calculations. However, DFT does provide the correct physical trends for both black phosphorus and $PdSe_2$.[21,45,51]

To further reveal the origin of the $\frac{\partial\omega}{\partial\varepsilon}$ with the uniaxial tensile strain, we examined the atomic structures of 1 - 3L $PdSe_2$ under the uniaxial tensile strain along different directions. The atomic displacements of the A_g^1 and A_g^3 modes of 1L $PdSe_2$ were illustrated in Supporting movie S1: both A_g^1 and A_g^3 are out-of-plane vibrational modes, and the phonon frequency of the A_g^1 mode is affected by the Se-Se bond and the two Pd-Se bonds (one Pd-Se bond roughly

along the *a*-axis and the other Pd-Se bond roughly along the *b*-axis, see **Figure 5** (A)), while the frequency of the A_g^3 mode is affected primarily by the Se-Se bond. Therefore, we calculated the changes of the three bond lengths with respect to the uniaxial tensile strain, as summarized in **Figure 5** (B-C)and **Table** 3. In general, with the uniaxial tensile strain applied to either axis, the Se-Se bond and the Pd-Se bond roughly along the strain direction are stretched; however, the Pd-Se bond approximately perpendicular to the strain direction is contracted. Recalling the near-zero Poisson's ratio of $PdSe_2$, the bond contraction perpendicular to the strain direction is significantly weaker than the bond stretching along the tensile strain (see **Table** 3), and hence the overall bond strengths are softened, leading to the general redshifts of corresponding Raman modes, as observed in both calculated and experimental data discussed above. More specifically, according to the calculations, for the A_g^3 mode that is mostly affected by the Se-Se bond, when the strain was applied along the *b*-axis, the change rate of the Se-Se bond length was about 3 folds of that under strain applied to the *a*-axis, causing a larger restoring force in the Se-Se bond and resulting in the larger $\left|\frac{\partial\omega}{\partial\varepsilon}\right|$ (about three folds) of the A_g^3 mode for $\varepsilon \parallel b$-axis. On the other hand, the $\frac{\partial\omega}{\partial\varepsilon}$ of the A_g^1 mode is affected by the changes of three bonds mentioned above. For the two Pd-Se bonds, one is approximately along the uniaxial tensile strain and stretched with the tensile strain (the bond length change rate is denoted as $L_{(Pd-Se)\,\parallel\,\varepsilon}$ in **Table** 3), while the other is roughly perpendicular to the tensile strain and contracted with the tensile strain (the bond length change rate is denoted as $L_{(Pd-Se)\,\perp\,\varepsilon}$). Due to the near-zero Poisson's ratio, the absolute value of $L_{(Pd-Se)\,\parallel\,\varepsilon}$ is significantly larger than that of $L_{(Pd-Se)\,\perp\,\varepsilon}$ as reflected by the ratio $\eta = \left|\frac{L_{(Pd-Se)\,\parallel\,\varepsilon}}{L_{(Pd-Se)\,\perp\,\varepsilon}}\right|$ shown in **Table** 3. When the uniaxial tensile strain was applied along the *a*-axis, η was ~18.18, which was much larger than that when the strain was applied along the *b*-axis ($\eta \approx 7.90$). Namely, compared to the case of $\varepsilon \parallel b$-axis, the Pd-Se bond stretching is much more significant than the Pd-Se bond contraction in the case of $\varepsilon \parallel a$-axis, resulting in the

relatively larger softening of the Pd-Se bond strengths and thus larger redshifts of the A_g^1 mode for ε ∥ *a*-axis.

Conclusion

In summary, we performed a comprehensive investigation of the anisotropic phonon responses of 2 – 5 L $PdSe_2$ under the uniaxial tensile strain. When the uniaxial tensile strain was along the *a*-axis of $PdSe_2$, the frequency change rate $\left|\frac{\partial\omega}{\partial\varepsilon}\right|$ of the A_g^1 mode was larger than that of the A_g^3 mode; however, when the uniaxial tensile strain was along the *b*-axis of $PdSe_2$, $\left|\frac{\partial\omega}{\partial\varepsilon}\right|$ of the A_g^3 mode was larger than that of the A_g^1 mode. Such an opposite trend was corroborated by first-principles DFT simulations, which reveal the microscopic origin of this unique phonon behavior under strain, i.e., the anisotropic length changes of the Pd-Se and Se-Se bonds. Under the uniaxial tensile strain along the *a*-axis, the larger $\left|\frac{\partial\omega}{\partial\varepsilon}\right|$ of the A_g^1 mode can be explained by the larger ratio η of the Pd-Se bond length change rate compared to when the uniaxial tensile strain was applied along the *b*-axis. However, under the uniaxial tensile strain along the *b*-axis, the larger $\left|\frac{\partial\omega}{\partial\varepsilon}\right|$ of the A_g^3 mode was attributed to the larger change rate of the Se-Se bond length. This anisotropic phonon response can be used for the determination of the crystal axes, complementary to the angle-dependent Raman intensities. Moreover, we found that few-layer $PdSe_2$ exhibits near-zero Poisson's ratios, leading to the effectively uniaxial tensile strain in the material. This is different from the biaxial strain induced in many other 2D materials when the external uniaxial tensile strain is applied. Thus, $PdSe_2$ offers a natural platform for the study of the uniaxial strain effect on physical properties. This work provided both experimental and theoretical insight in the Raman scattering of strained few-layer $PdSe_2$, unveiling it to be the first anisotropic 2D material with near-zero Poisson's ratio, and enabling diverse possibilities for the strain engineering of electrical, optical and thermal properties in $PdSe_2$.

Experimental Section

Sample preparation: $PdSe_2$ thin flakes were first mechanically exfoliated onto a 300 nm SiO_2/Si wafer using Nitto SPV 224R blue tape from bulk $PdSe_2$ single crystal that was synthesized using a self-flux method.[21] The angle-resolved Raman measurements were performed to find and distinguish the two main axes (i.e., *a* and *b* axes) of the few-layer $PdSe_2$ flake. The few-layer $PdSe_2$ flakes were picked up using the method similar to previous work.[58] Briefly, polystyrene (PS) solution (1:9 dissolved in Toluene) was spin-coated uniformly onto a SiO_2/Si substrate and cured at 70 ℃ for 20 minutes. Then the PS thin film carrying the few-layer $PdSe_2$ flakes was delaminated from the substrate in the deionized (DI) water by poking the edge of the film. After that, a clean fresh-made PDMS film was used to pick up the PS thin film that was floating on the water. The PDMS-PS stamp was transferred onto the center of a cross-shaped Kapton polyimide film, with the two main crystal axes of the few-layer $PdSe_2$ pointing to the two directions of the cross, respectively. This process was performed under a microscope, similar to that of stacking 2D Van der Waals heterostructures.[59] Lastly, the few-layer $PdSe_2$ fully conformed on the polyimide film via hydrogen bonding and the interface interaction was further enhanced through a two-step annealing process (first at 70 ℃ for 20 min, and then, after removal of the polystyrene stamp in toluene, at 80 ℃ for two hours).[60] The overall procedure is also shown in **Figure S14** in the SI (**Section** S5). The tensile strain was loaded using a homemade stretching fixture (see the inset optical image in **Figure** S14) similar to Zhu et al.'s work,[45] in which two ends of the long cross-shaped Polyimide substrate (Dupont Kapton HN, 50-μm-thick) were mounted across the two clamps of the stretcher. The measurements of the initial distance and elongation of the Kapton film were performed by a caliper, and the results were used for the strain calculation.

Raman spectra measurements: Raman spectroscopy measurements were performed on a Horiba T64000 micro-Raman system with a back-scattering configuration using a 532 nm wavelength

excitation. To avoid the laser damage, the laser power density was minimized to be < 0.2 mW/μm^2. The samples were rotated with respect to the incident polarization via a motorized continuous rotation stage (SIGMAKOKI SGSP-120YAW) with a positioning accuracy of 0.1°. All spectra were collected under a 100× magnification objective with an NA = 0.85, resulting in a beam spot ~0.8 μm in diameter. A spectrum resolution of ~ 0.6 cm^{-1} was achieved using a 1800 lines/mm grating.

DFT calculation: Plane-wave DFT calculations were carried out using the Vienna Ab initio Simulation Package (55,56) (VASP) with projector augmented wave (PAW) pseudopotentials [61,63,64] for electron-ion interactions and the optPBE-vdW [65] (optPBE) functional for exchange-correlation interactions. Prior works [21,51] demonstrated that the optPBE functional offers reasonable results of the electronic and structural properties of few-layer $PdSe_2$. Based on the bulk $PdSe_2$ structure (Materials-project database [52]), the original strain-free 1 - 3L $PdSe_2$ was modeled by creating a periodic slab with a vacuum separation of more than 22 Å to avoid the interactions with periodic images in the out-of-plane direction (Z direction). A cutoff energy of 350 eV and 12×12×1 k-point samplings were used for the optimization of the unit cell (both atomic positions and in-plane lattice constants) until the maximum force allowed on each atom was less than 0.001eV / Å. The total volume of the structures was fixed during geometry optimization to avoid the structural collapse of the 2D slabs with vacuum separations. For 1 – 3L $PdSe_2$, different uniaxial tensile strains (0.83% increment, and up to 5.00%) were introduced along the $PdSe_2$ *a* and *b* axes, respectively. Note that when the tensile strain was applied to one in-plane direction, the lattice constant along the other in-plane direction generally tends to contract slightly. Therefore, the stable strained structures were obtained by adding different compressions to the direction that was perpendicular to the strain and searching for the geometry with the lowest total energy. The Poisson's ratios of 1 – 3L $PdSe_2$ can also be obtained via this approach.

Based on the fully relaxed geometries, the phonon frequencies were then calculated using the finite difference scheme implemented in the Phonopy software.[66] The visualization of the mode displacement was realized by ascii-phonon package.[67] In addition, the Raman spectra of 2L and 3L $PdSe_2$ were calculated via the following approach: after the strained structures were fully relaxed, the Hellmann−Feynman forces (the second-order force constants) of a 2×2×1 supercell were computed by VASP for both positive and negative atomic displacements (δ = 0.03 Å), and then used in Phonopy code to construct the dynamic matrices. Then the phonon frequencies and eigenvectors could be obtained after the diagonalization of the dynamic matrices. The phonon spectral linewidth at room temperature (T = 300 K) for the j-th Raman mode was generated from the third-order force calculations by Phono3py code.[68] In addition, the Born effective-charge tensors and dielectric constant tensors were also calculated using the density-functional perturbation theory [66] (DFPT) routines in VASP. Later, the intensities of Raman modes can be calculated from the derivatives of the polarizability tensor (macroscopic dielectric tensor) along the normal mode coordinate, which can be interpreted as:[69]

$$I_{\mathrm{Raman},\alpha\beta}(s) = \frac{\Omega}{4\pi}\left[-\frac{1}{2}\frac{\varepsilon^{\infty}_{\alpha\beta}(-s)}{\Delta Q(s)} + \frac{1}{2}\frac{\varepsilon^{\infty}_{\alpha\beta}(s)}{\Delta Q(s)}\right], \quad (1)$$

At last, the simulated Raman spectra were generated by the Phonopy-spectroscopy code.[67]

Supporting Information

Supporting Information is available from the Wiley Online Library or from the author.

Acknowledgments

This material is based upon work supported by the National Science Foundation (NSF) under Grant No.(1945364). X. L. acknowledges the membership of the Photonics Center at Boston University. W. L. acknowledge the high-performance computing resources of the Boston University Shared Computing Cluster (SCC). L.L., A.D.O., Y.G., A.P., and K.X. acknowledge work conducted at the Center for Nanophase Materials Sciences, which is a US Department of Energy Office of Science User Facility. A.D.O acknowledges support from the Bredesen Center, University of Tennessee, Knoxville.

Received: ((will be filled in by the editorial staff))
Revised: ((will be filled in by the editorial staff))
Published online: ((will be filled in by the editorial staff))

References

[1] X. Ling, H. Wang, S. Huang, F. Xia, M. S. Dresselhaus, *Proceedings of the National Academy of Sciences* **2015**, 201416581.

[2] X. Ling, S. Huang, E. H. Hasdeo, L. Liang, W. M. Parkin, Y. Tatsumi, A. R. Nugraha, A. A. Puretzky, P. M. Das, B. G. Sumpter, *Nano letters* **2016**, *16*, 2260.

[3] D. A. Chenet, O. B. Aslan, P. Y. Huang, C. Fan, A. M. van der Zande, T. F. Heinz, J. C. Hone, *Nano letters* **2015**, *15*, 5667.

[4] Y.-C. Lin, H.-P. Komsa, C.-H. Yeh, T. Bjorkman, Z.-Y. Liang, C.-H. Ho, Y.-S. Huang, P.-W. Chiu, A. V. Krasheninnikov, K. Suenaga, *ACS nano* **2015**, *9*, 11249.

[5] D. Wolverson, S. Crampin, A. S. Kazemi, A. Ilie, S. J. Bending, *ACS nano* **2014**, *8*, 11154.

[6] C. Xin, J. Zheng, Y. Su, S. Li, B. Zhang, Y. Feng, F. Pan, *The Journal of Physical Chemistry C* **2016**, *120*, 22663.

[7] L. Li, Z. Chen, Y. Hu, X. Wang, T. Zhang, W. Chen, Q. Wang, *Journal of the American Chemical Society* **2013**, *135*, 1213.

[8] S. Yang, Y. Yang, M. Wu, C. Hu, W. Shen, Y. Gong, L. Huang, C. Jiang, Y. Zhang, P. M. Ajayan, *Advanced Functional Materials* **2018**, *28*, 1707379.

[9] D. Tan, H. E. Lim, F. Wang, N. B. Mohamed, S. Mouri, W. Zhang, Y. Miyauchi, M. Ohfuchi, K. Matsuda, *Nano Research* **2017**, *10*, 546.

[10] Y. Hu, S. Zhang, S. Sun, M. Xie, B. Cai, H. Zeng, *Applied Physics Letters* **2015**, *107*, 122107.

[11] M. Yagmurcukardes, H. Sahin, J. Kang, E. Torun, F. M. Peeters, R. T. Senger, *Journal of Applied Physics* **2015**, *118*, 104303.

[12] J. Tao, W. Shen, S. Wu, L. Liu, Z. Feng, C. Wang, C. Hu, P. Yao, H. Zhang, W. Pang, *ACS nano* **2015**, *9*, 11362.

[13] W. Zhu, M. N. Yogeesh, S. Yang, S. H. Aldave, J.-S. Kim, S. Sonde, L. Tao, N. Lu, D. Akinwande, *Nano letters* **2015**, *15*, 1883.

[14] L.-D. Zhao, S.-H. Lo, Y. Zhang, H. Sun, G. Tan, C. Uher, C. Wolverton, V. P. Dravid, M. G. Kanatzidis, *Nature* **2014**, *508*, 373.

[15] Z. Luo, J. Maassen, Y. Deng, Y. Du, R. P. Garrelts, M. S. Lundstrom, D. Y. Peide, X. Xu, *Nature communications* **2015**, *6*, 8572.

[16] S. Tongay, H. Sahin, C. Ko, A. Luce, W. Fan, K. Liu, J. Zhou, Y.-S. Huang, C.-H. Ho, J. Yan, *Nature communications* **2014**, *5*, 3252.

[17] H. Jang, C. R. Ryder, J. D. Wood, M. C. Hersam, D. G. Cahill, *Advanced Materials* **2017**, *29*, 1700650.

[18] S. Zhang, J. Yang, R. Xu, F. Wang, W. Li, M. Ghufran, Y.-W. Zhang, Z. Yu, G. Zhang, Q. Qin, *ACS nano* **2014**, *8*, 9590.

[19] D.-J. Xue, J. Tan, J.-S. Hu, W. Hu, Y.-G. Guo, L.-J. Wan, *Advanced Materials* **2012**, *24*, 4528.

[20] T. Low, M. Engel, M. Steiner, P. Avouris, *Physical Review B* **2014**, *90*, 081408.

[21] A. D. Oyedele, S. Yang, L. Liang, A. A. Puretzky, K. Wang, J. Zhang, P. Yu, P. R. Pudasaini, A. W. Ghosh, Z. Liu, *Journal of the American Chemical Society* **2017**, *139*, 14090.

[22] W. L. Chow, P. Yu, F. Liu, J. Hong, X. Wang, Q. Zeng, C.-H. Hsu, C. Zhu, J. Zhou, X. Wang, *Advanced Materials* **2017**, *29*, 1602969.

[23] A. D. Oyedele, S. Yang, T. Feng, A. V. Haglund, Y. Gu, A. A. Puretzky, D. Briggs, C. M. Rouleau, M. F. Chisholm, R. R. Unocic, *Journal of the American Chemical Society* **2019**, *141*, 8928.
[24] W. Lei, S. Zhang, G. Heymann, X. Tang, J. Wen, X. Zheng, G. Hu, X. Ming, *Journal of Materials Chemistry C* **2019**, *7*, 2096.
[25] T. S. Walmsley, K. Andrews, T. Wang, A. Haglund, U. Rijal, A. Bowman, D. Mandrus, Z. Zhou, Y.-Q. Xu, *Nanoscale* **2019**, *11*, 14410.
[26] D. Qin, P. Yan, G. Ding, X. Ge, H. Song, G. Gao, *Scientific reports* **2018**, *8*, 2764.
[27] N. Mao, J. Tang, L. Xie, J. Wu, B. Han, J. Lin, S. Deng, W. Ji, H. Xu, K. Liu, others, *J. Am. Chem. Soc.* **2016**, *138*, 300.
[28] J. Wu, N. Mao, L. Xie, H. Xu, J. Zhang, *Angewandte Chemie International Edition* **2015**, *54*, 2366.
[29] S. Zhang, N. Mao, J. Wu, L. Tong, J. Zhang, Z. Liu, *Small* **2017**, *13*, 1700466.
[30] P. H. Tan, W. P. Han, W. J. Zhao, Z. H. Wu, K. Chang, H. Wang, Y. F. Wang, N. Bonini, N. Marzari, N. Pugno, *Nature materials* **2012**, *11*, 294.
[31] X.-F. Qiao, J.-B. Wu, L. Zhou, J. Qiao, W. Shi, T. Chen, X. Zhang, J. Zhang, W. Ji, P.-H. Tan, *Nanoscale* **2016**, *8*, 8324.
[32] X. Zhang, W. P. Han, J. B. Wu, S. Milana, Y. Lu, Q. Q. Li, A. C. Ferrari, P. H. Tan, *Physical Review B* **2013**, *87*, 115413.
[33] H. Zhao, J. Wu, H. Zhong, Q. Guo, X. Wang, F. Xia, L. Yang, P. Tan, H. Wang, *Nano Research* **2015**, *8*, 3651.
[34] Y. Zhao, X. Luo, H. Li, J. Zhang, P. T. Araujo, C. K. Gan, J. Wu, H. Zhang, S. Y. Quek, M. S. Dresselhaus, *Nano letters* **2013**, *13*, 1007.
[35] Y. Zhao, X. Luo, J. Zhang, J. Wu, X. Bai, M. Wang, J. Jia, H. Peng, Z. Liu, S. Y. Quek, *Physical Review B* **2014**, *90*, 245428.
[36] X. Ling, L. Liang, S. Huang, A. A. Puretzky, D. B. Geohegan, B. G. Sumpter, J. Kong, V. Meunier, M. S. Dresselhaus, *Nano letters* **2015**, *15*, 4080.
[37] X. Luo, X. Lu, G. K. W. Koon, A. H. Castro Neto, B. Özyilmaz, Q. Xiong, S. Y. Quek, *Nano letters* **2015**, *15*, 3931.
[38] Y. Zhao, J. Qiao, P. Yu, Z. Hu, Z. Lin, S. P. Lau, Z. Liu, W. Ji, Y. Chai, *Advanced Materials* **2016**, *28*, 2399.
[39] L. Liang, J. Zhang, B. G. Sumpter, Q.-H. Tan, P.-H. Tan, V. Meunier, *ACS nano* **2017**, *11*, 11777.
[40] X. Peng, Q. Wei, A. Copple, *Physical Review B* **2014**, *90*, 085402.
[41] C. Rice, R. J. Young, R. Zan, U. Bangert, D. Wolverson, T. Georgiou, R. Jalil, K. S. Novoselov, *Physical Review B* **2013**, *87*, 081307.
[42] T. M. G. Mohiuddin, A. Lombardo, R. R. Nair, A. Bonetti, G. Savini, R. Jalil, N. Bonini, D. M. Basko, C. Galiotis, N. Marzari, *Physical Review B* **2009**, *79*, 205433.
[43] Y. Wang, C. Cong, C. Qiu, T. Yu, *Small* **2013**, *9*, 2857.
[44] Z. H. Ni, T. Yu, Y. H. Lu, Y. Y. Wang, Y. P. Feng, Z. X. Shen, *ACS nano* **2008**, *2*, 2301.
[45] W. Zhu, L. Liang, R. H. Roberts, J.-F. Lin, D. Akinwande, *ACS Nano* **2018**.
[46] M. Huang, H. Yan, T. F. Heinz, J. Hone, *Nano letters* **2010**, *10*, 4074.
[47] M. Yagmurcukardes, C. Bacaksiz, E. Unsal, B. Akbali, R. T. Senger, H. Sahin, *Physical Review B* **2018**, *97*, 115427.
[48] A. M. Dadgar, D. Scullion, K. Kang, D. Esposito, E.-H. Yang, I. P. Herman, M. A. Pimenta, E.-J. Santos, A. N. Pasupathy, *Chemistry of Materials* **2018**, *30*, 5148.
[49] S. Yang, C. Wang, H. Sahin, H. Chen, Y. Li, S.-S. Li, A. Suslu, F. M. Peeters, Q. Liu, J. Li, *Nano letters* **2015**, *15*, 1660.
[50] L. Li, W. Han, L. Pi, P. Niu, J. Han, C. Wang, B. Su, H. Li, J. Xiong, Y. Bando, *InfoMat* **2019**, *1*, 54.

[51] A. A. Puretzky, A. D. Oyedele, K. Xiao, A. V. Haglund, B. G. Sumpter, D. Mandrus, D. B. Geohegan, L. Liang, *2D Materials* **2018**, *5*, 035016.
[52] A. Jain, S. P. Ong, G. Hautier, W. Chen, W. D. Richards, S. Dacek, S. Cholia, D. Gunter, D. Skinner, G. Ceder, *Apl Materials* **2013**, *1*, 011002.
[53] Y. Du, J. Maassen, W. Wu, Z. Luo, X. Xu, P. D. Ye, *Nano letters* **2016**, *16*, 6701.
[54] G. Liu, Q. Zeng, P. Zhu, R. Quhe, P. Lu, *Computational Materials Science* **2019**, *160*, 309.
[55] A. Mogulkoc, Y. Mogulkoc, A. N. Rudenko, M. I. Katsnelson, *Physical Review B* **2016**, *93*, 085417.
[56] R. Schmidt, I. Niehues, R. Schneider, M. Drüppel, T. Deilmann, M. Rohlfing, S. M. De Vasconcellos, A. Castellanos-Gomez, R. Bratschitsch, *2D Materials* **2016**, *3*, 021011.
[57] R. Roldán, A. Castellanos-Gomez, E. Cappelluti, F. Guinea, *Journal of Physics: Condensed Matter* **2015**, *27*, 313201.
[58] A. Gurarslan, Y. Yu, L. Su, Y. Yu, F. Suarez, S. Yao, Y. Zhu, M. Ozturk, Y. Zhang, L. Cao, *ACS nano* **2014**, *8*, 11522.
[59] C.-H. Lee, G.-H. Lee, A. M. Van Der Zande, W. Chen, Y. Li, M. Han, X. Cui, G. Arefe, C. Nuckolls, T. F. Heinz, *Nature nanotechnology* **2014**, *9*, 676.
[60] X. Wang, X. Cui, A. Bhat, D. E. Savage, J. L. Reno, M. G. Lagally, R. Paiella, *Applied Physics Letters* **2018**, *113*, 201105.
[61] G. Kresse, *Phys. Rev. B* **1996**, *54*, 11169.
[62] G. Kresse, J. Furthmüller, *Computational materials science* **1996**, *6*, 15.
[63] J. P. Perdew, *Phys. Rev. Lett.* **2008**, *100*, 136406.
[64] J. P. Perdew, *Phys. Rev. Lett.* **1996**, *77*, 3865.
[65] M. Dion, H. Rydberg, E. Schröder, D. C. Langreth, B. I. Lundqvist, *Physical review letters* **2004**, *92*, 246401.
[66] A. Togo, F. Oba, I. Tanaka, *Physical Review B* **2008**, *78*, 134106.
[67] J. Skelton, *A Collection of Tools for Simulating Vibrational Spectra, Which Interfaces with the Phonopy Package.: JMSkelton/Phonopy-Spectroscopy*, **2019**.
[68] A. Togo, L. Chaput, I. Tanaka, *Physical Review B* **2015**, *91*, 094306.
[69] J. M. Skelton, L. A. Burton, A. J. Jackson, F. Oba, S. C. Parker, A. Walsh, *Physical Chemistry Chemical Physics* **2017**, *19*, 12452.

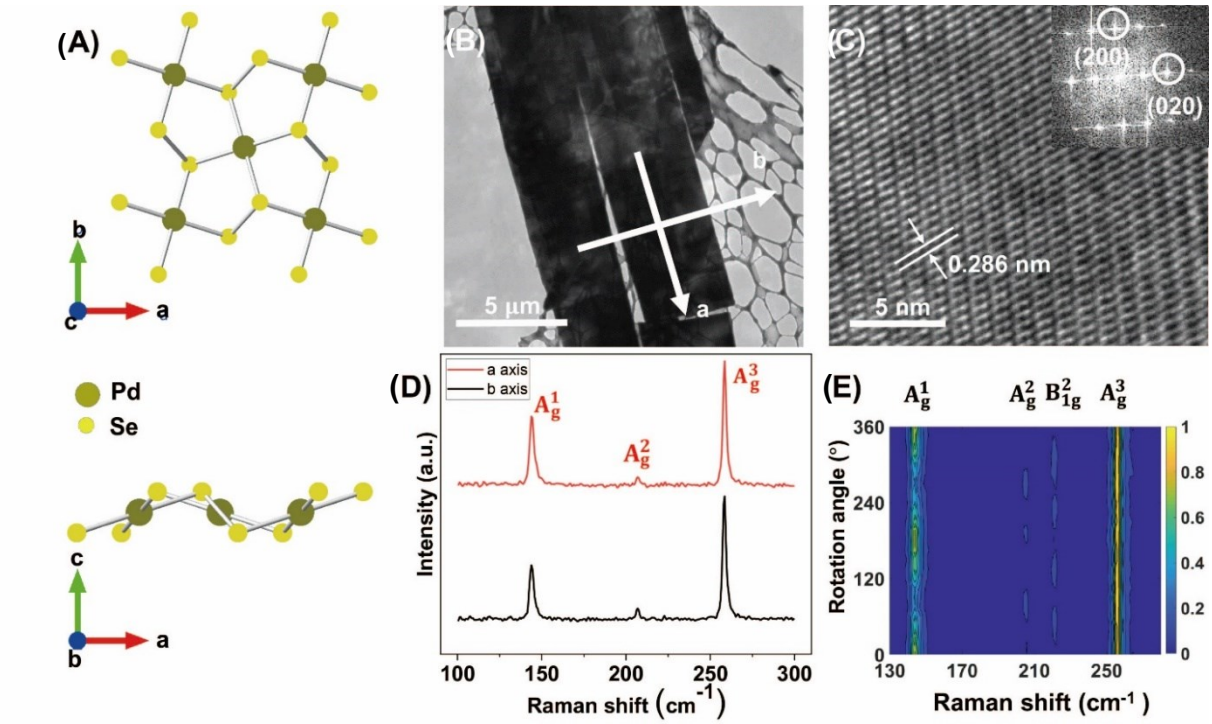

Figure 1. (A) The crystallographic structure of a 1L 2D pentagonal $PdSe_2$. (B) Low-magnification TEM image of a typical exfoliated $PdSe_2$ flake (> 20 L). (C) An atomic resolution TEM image of the exfoliated $PdSe_2$ flake and the inset shows the FFT of the image with (200) and (020) planes labeled, indicating the *a* and *b* axes, respectively. (D) Raman spectra collected with the incident light polarization parallel to the *a*- and *b*-axis, respectively (note that the scattered light polarization is the same as the incident light polarization). (E) Contour color map of the angle-resolved Raman spectra of the $PdSe_2$ flake.

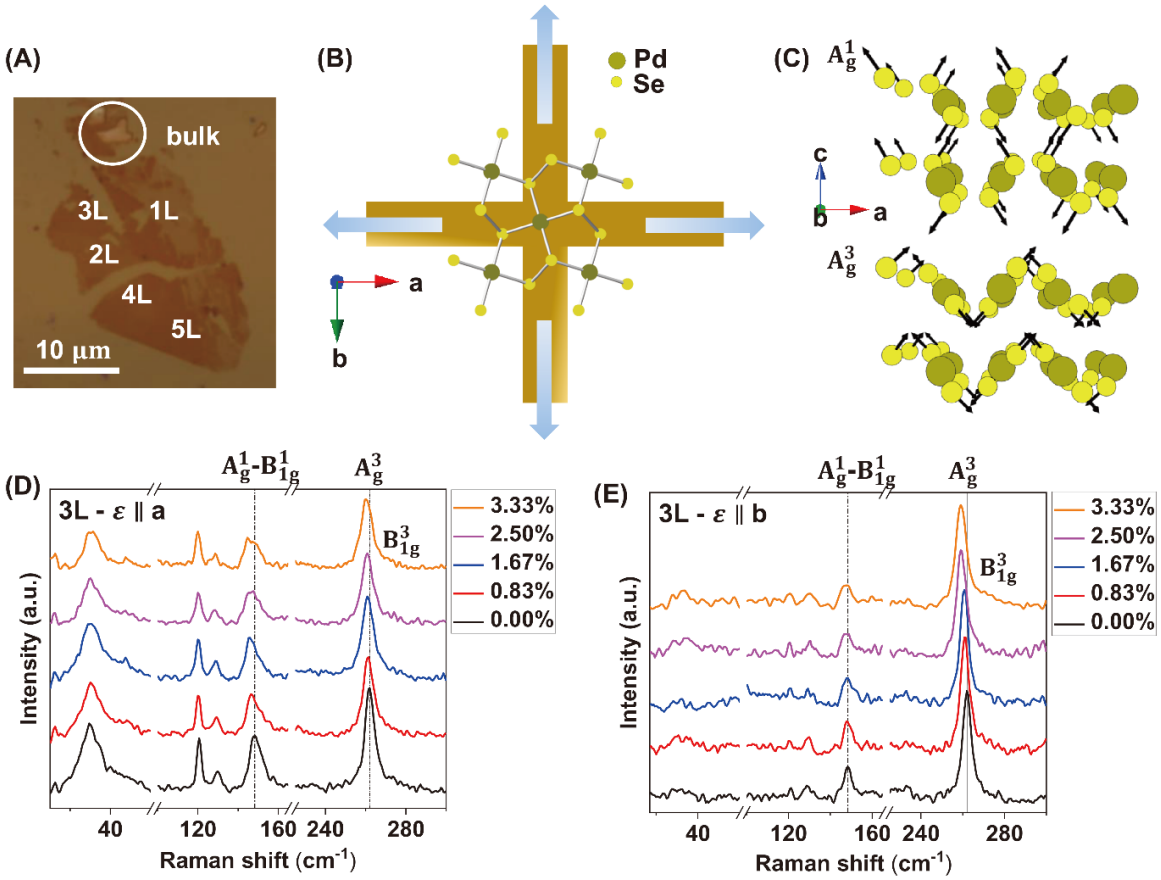

Figure 2. (A) The optical image of a $PdSe_2$ sample on a 300 nm SiO_2/Si substrate. (B) Illustration of uniaxial strain applied to the different directions of the $PdSe_2$ sample shown in (A) after transfer onto a cross–shape flexible polyimide substrate. (C) Illustration of atomic displacements of A_g^1 and A_g^3 modes. (D) and (E) Raman spectra of the 3L $PdSe_2$ flake collected under the uniaxial tensile strain along the *a*-axis (denoted as ε||*a*) and *b*-axis (denoted as ε||*b*), respectively.

Table 1. Summary of the experimental frequency change rates of A_g^1 and A_g^3 modes of 2 – 5 L $PdSe_2$ with strain.

Layer number	ε ∥ 0° (*a*-axis)		ε ∥ 90° (*b*-axis)	
	$\frac{\partial\omega}{\partial\varepsilon}$ (cm^{-1}/%)			
	A_g^1	A_g^3	A_g^1	A_g^3
2 L	-0.71	-0.40	/	-0.60
3 L	-0.97	-0.38	-0.25	-0.74
4 L	-1.47	-0.67	-0.22	-0.69
5 L	-1.46	-0.81	-0.10	-0.66

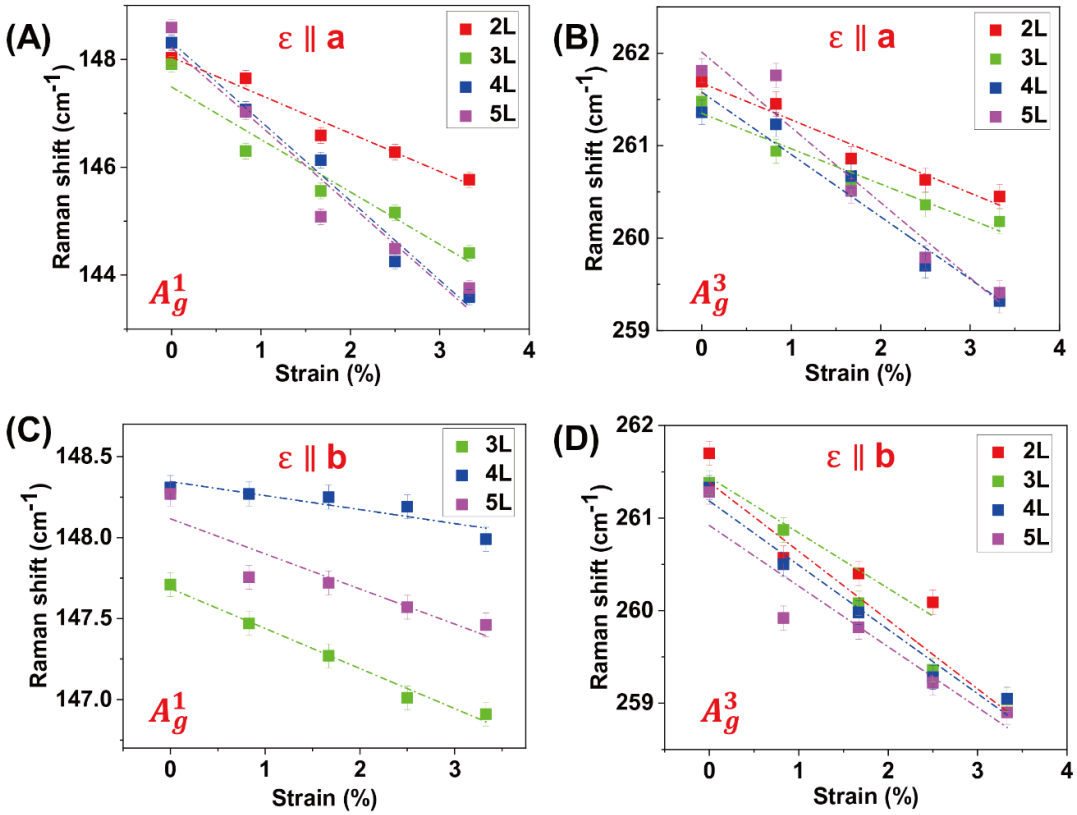

Figure 3. The experimental Raman shifts as a function of the uniaxial tensile strain applied to few-layer $PdSe_2$. (A) and (B) Raman shifts of the A_g^1 and A_g^3 modes when the uniaxial tensile strain was applied to the $PdSe_2$ *a*-axis, respectively. (C) and (D) Raman shifts of the A_g^1 and A_g^3 modes when the uniaxial tensile strain was applied to the $PdSe_2$ *b*-axis, respectively. The error bars indicate a fitting uncertainty of 0.2 cm^{-1}.

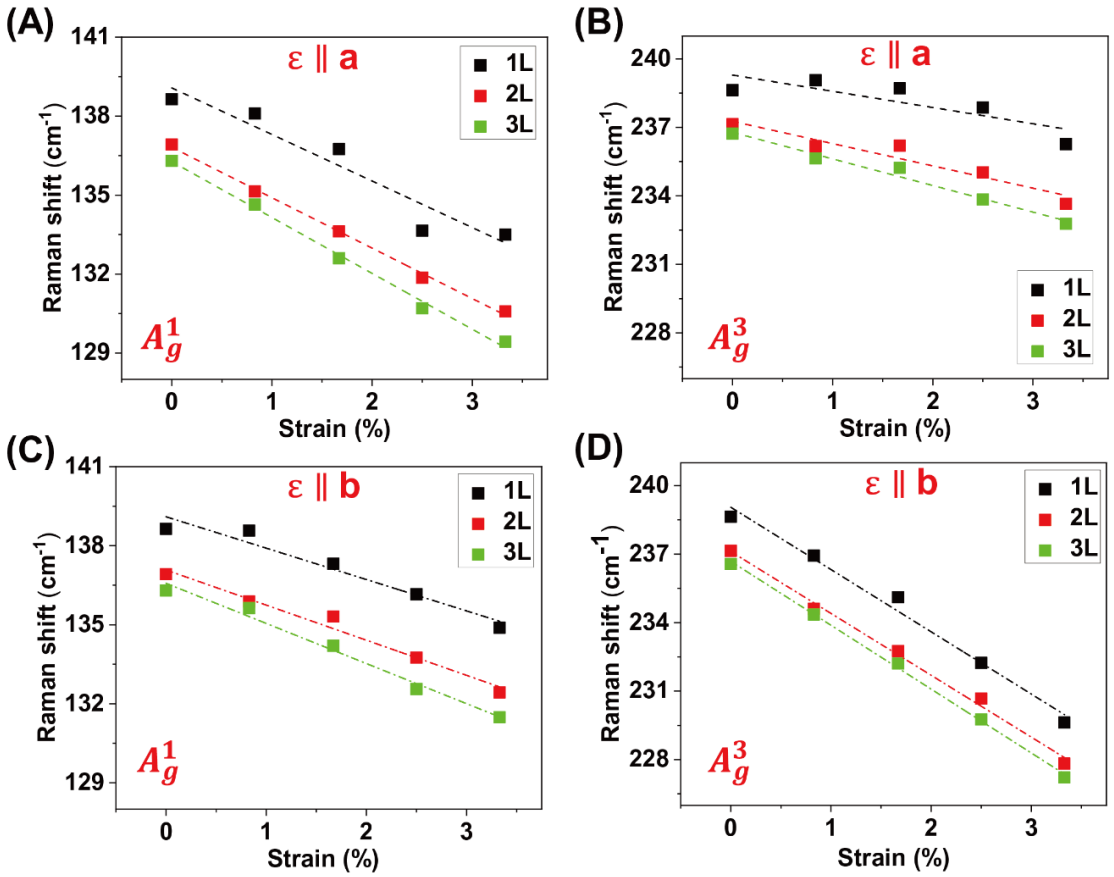

Figure 4. The simulated Raman shifts of 1 – 3 L $PdSe_2$ as a function of strain. (A) and (B) the frequency changes of A_g^1 and A_g^3 modes under the uniaxial tensile strain along the $PdSe_2$ *a*-axis, respectively; (C) and (D) the frequency changes of A_g^1 and A_g^3 modes under the uniaxial tensile strain along the $PdSe_2$ *b*-axis, respectively.

Table 2. Summary of the simulated frequency change rates of A_g^1 and A_g^3 modes of 1 – 3 L $PdSe_2$ with strain.

Layer number	ε ∥ 0° (*a*-axis)		ε ∥ 90° (*b*-axis)	
	$\frac{\partial\omega}{\partial\varepsilon}$ (cm^{-1}/%)			
	A_g^1	A_g^3	A_g^1	A_g^3
1 L	-1.77	-0.71	-1.19	-2.65
2 L	-1.92	-0.98	-1.33	-2.71
3 L	-2.12	-1.16	-1.52	-2.80

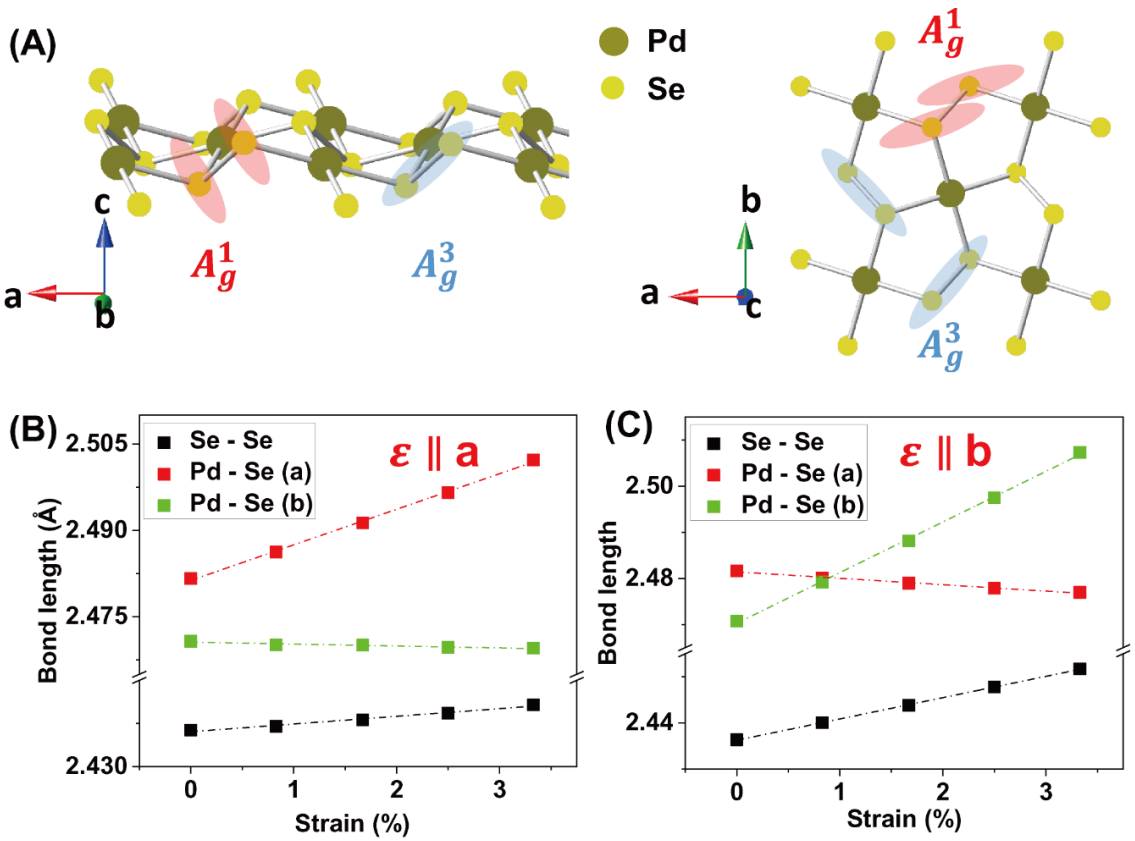

Figure 5. The analysis of bond length changes under strain. (A) Side and top views of the crystallographic structure of monolayer $PdSe_2$: the red and blue ellipses indicate the atomic displacement of A_g^1 and A_g^3 modes, respectively. More details of the mode displacements can be seen in the Supporting Movie 1. (B) Calculated bond length change under strain applied to *a*-axis. (C) Calculated bond length change under strain applied to the *b*-axis.

Table 3. Calculated change rates of the bond lengths ($\frac{\partial L}{\partial \varepsilon}$) of 1L $PdSe_2$ with respect to the uniaxial tensile strain. We have considered two Pd-Se bonds and one Se-Se bond (**Figure** 5 (A)). For the two Pd-Se bonds, one is approximately along the uniaxial tensile strain and elongated with the tensile strain (the bond length change rate is denoted as $L_{(Pd-Se)\parallel \varepsilon}$), while the other is roughly perpendicular to the tensile strain and contracted with the tensile strain (the bond length change rate is denoted as $L_{(Pd-Se)\perp \varepsilon}$). Recalling the near-zero Poisson's ratio of $PdSe_2$, the absolute value of $L_{(Pd-Se)\parallel \varepsilon}$ is significantly larger than that of $L_{(Pd-Se)\perp \varepsilon}$, as reflected by the ratio $\eta = |\frac{L_{(Pd-Se)\parallel \varepsilon}}{L_{(Pd-Se)\perp \varepsilon}}|$. Note that there are also two kinds of Se-Se bonds shown in **Figure 5** (A): one (the other) is aligned roughly 45° (135°) with respect to the uniaxial tensile strain. Therefore, the two Se-Se bonds exhibit the same response to the strain, and hence only the data of one bond is shown.

	$\frac{\partial L_{(Pd-Se)}}{\partial \varepsilon}$(Å/%)			$\frac{\partial L_{(Se-Se)}}{\partial \varepsilon}$(Å/%)
Strain Direction	$L_{(Pd-Se)\parallel \varepsilon}$	$L_{(Pd-Se)\perp \varepsilon}$	$\eta = \lvert\frac{L_{(Pd-Se)\parallel \varepsilon}}{L_{(Pd-Se)\perp \varepsilon}}\rvert$	
$\varepsilon \parallel$ *a*-axis	0.00618	-0.00034	~ 18.18	0.00133
$\varepsilon \parallel$ *b*-axis	0.01098	-0.00139	~ 7.90	0.00462